RSC Advances

pH-responsive nanovalves based on encapsulated halloysite for controlled release of corrosion inhibitor in epoxy coating

Journal:	*RSC Advances*
Manuscript ID	RA-ART-09-2015-019296.R1
Article Type:	Paper
Date Submitted by the Author:	01-Oct-2015
Complete List of Authors:	He, Yi; Southwest Petroleum University, Xu, Wei; Southwest Petroleum University, Tang, Ran; Southwest Petroleum University, Zhang, Chunli; Southwest Petroleum University, Yang, Qiangbing; Southwest Petroleum University, School of Chemistry and Chemical Engineering, Southwest Petroleum University
Subject area & keyword:	Encapsulation < Materials

pH-responsive nanovalves based on encapsulated halloysite for controlled release of corrosion inhibitor in epoxy coating

Yi He [a,b,c*], Wei Xu[b,c], Ran Tang[b,c], Chunli Zhang[b,c], Qiangbin Yang[b,c]

(a. State Key Laboratory of Oil & Gas Reservoir Geology and Exploitation, Southwest Petroleum University, Chengdu, Sichuan 610500, P R of China; b. College of Chemistry and Chemical Engineering, Southwest Petroleum University, Chengdu,Sichuan 610500, P R of China; c. Oil & Gas Field Applied Chemistry Key Laboratory of Sichuan Province, Southwest Petroleum University, Chengdu, Sichuan 610500, P R of China)

*Address correspondence to this author. E-mail: heyi007@163.com; Tel: 86-13518112988; Fax: 86-028-83037315

Abstract: Halloysite nanotubes (HNTs) were applied as corrosion inhibitor (benzotriazole, BTA) hosts, which were encapsulated by using tetraethyl orthosilicate (TEOS) and modified by (3-aminopropyl)triethoxysilane (APTES), respectively. The modified nanocontainers were dispersed in the epoxy matrix, resulting in a functional composite coating. The structure of assembly of modified HNTs was characterized by FT-IR, XRD, XPS and TEM. Furthermore, the content of BTA loaded in lumen of HNTs was determined by TGA. Such modified HNTs were well dispersed in ethanol and epoxy resin which was confirmed by SEM and EDS. A reasonable release rate of the corrosion inhibitor from nanocontainer was realized by controlling pH value (pH=3) and monitoring range of UV-vis between 30 and 450 min. Compare to the pure epoxy coating, the anticorrosive performance of coating loaded with 3% of HNTs-entrapped BTA was tested by EIS method on steel matrix (N80) and showed remarkable improvement. Furthermore, the simulating inhibiting behaviors of

inhibitor releasing from nanocontainer in composite coatings was investigated by scarification test in 10 wt% NaCl solution (pH=3). The result demonstrated that the corrosion inhibitor releasing nanocontainer played a key role in protecting substrate.

Keywords: Halloysite nanotubes; corrosion inhibitor; hosts; epoxy matrix; anticorrosive performance; inhibiting behaviors

1. Introduction

Metal is one of the most common materials that used in industry and daily life. However, the corrosion of metal can cause great loss of economy and serious environmental problem. Several methods such as organic/inorganic coating, corrosion inhibitor or others have been successfully adopted to solve this problem [1-9]. Nonetheless, in order to protect metal substrate in aggressive medium such as saline solution, individual application of above methods cannot meet the requirements in marine industry. It is well-accepted that the organic coating which is mainly made of thermosetting resins is a common method to be used in field of corrosion protection. But, some volatiles (solvent, water and curing products) would release from the thermosetting coatings such as epoxy coating during the process of curing, which would cause many defects in coating such as mocroholes and crack[10, 11]. Thus, chlorine ions can easily penetrated into the coatings through the tiny holes or crack, which decreases the corrosive resistance of protective layer in aggressive environments.

To solve these problems, many researchers proposed several new methods [12-15]. Among these, incorporation of inhibitor into the organic coating to resist the invasion of corrosive medium is an effective and simple method [16, 17]. For this purpose,

using BTA as corrosion inhibitor is excellent choice because it is environmental friendly and cost effective. Besides, its derivatives are among the most effective inhibitors that used for protection of metals, especially for transition metals [18-20]. However, once the coating containing corrosion inhibitor contacts with corrosive medium, the BTA as water-soluble organic matter is easily dissolved in solution, which also cause the micropores in the coating[21]. Recent research showed that encapsulation of corrosion inhibitors into inner lumen of nanoparticles is a perspective method. Dmitri Fix and coworkers reported the anticorrosive agents encapsulated HNTs which were dispersed into a SiO_x–ZrO_x hybrid film [22]. It was found that the corrosion inhibitor releasing from nanocontainer resulted in corrosion inhibiting action at damage area, which rapidly decreased maximal anodic activity. However, there is no a stopper or barrier to control the anticorrosive agents releasing from nanocontainer. Therefore, during the preparation of anticorrosive coating, the agents could release from nanocontainer. Elshad Abdullayev and coworkers successfully prepared the stoppers (Cu–BTA complex) at the tube openings of HNTs which capsulated corrosion inhibitors[23]. The container with an encapsulation of BTA significantly increased the inhibitive performance of oil-based blue paint.

The halloysite which has an empty inner lumen in the sub-micrometer range is defined as a multi-walled aluminosilicate with the ideal chemical formula of $Al_2Si_2O_5(OH)_4•2H_2O$. In general, the length and inner diameter of HNTs are between 1–15μm and 10–150 nm, respectively. HNTs as natural nanocontainer encapsulating corrosion inhibitor have great promise for practical application. Because the

nanotubes are available in thousands of tons and nontoxic to environment [24, 25]. However, HNTs as nanometer materials cannot be well dispersed in aqueous/organic solvents due to the strong van der Waals force attraction among themselves [26, 27]. Therefore, it is necessary to modify the surface of nanocontainer. But, due to the multi-layer structure, most of the hydroxyl groups are inner groups and only a few hydroxyl groups are located on the surface of HNTs [28]. So, direct surface modification of HNTs is difficult. Meanwhile, the corrosion inhibitor releasing from hosts should be controlled in a certain speed range, which can maintain high anticorrosion performance of coatings in long-term period.

In this paper, HNTs as nanocontainer dispersed in epoxy coating for sustained release of BTA was reported. Extended controlled release was achieved by coating of TEOS film to form a microcapsule packing nanocontainer. The introduction of the outer TEOS film not only encapsulated the inner nanocontainer but also provided reaction sites for further functionalization with amine groups by APTES, which can get a good dispersion of nanometer materials in epoxy coating[29, 30]. Meanwhile, because of the fact that TEOS film can be gradually damaged depending on the pH values (pH=1, 3, 5), a simple method provided tunable release rate of the corrosion inhibitor. The release time of BTA is between 30 min and 450 min under a magnetic stirring at a constant rotational speed. These clay nanocontainers containing BTA were determined to improve the anticorrosion performance of coatings in long-term, supervised by EIS method in 3.5% NaCl solution (pH=3). Furthermore, scarification test was utilized to simulate the inhibiting behaviors of corrosion inhibitor in 10 wt%

NaCl solution (pH=3).

2. Experimental section

2.1 Materials and equipments

HNTs were provided by Hubei mineral ($Al_2Si_2O_5(OH)_4•2H_2O$). All the following reagents were provide by Chengdu Kelong Chemical Co., Ltd. TEOS (Tetraethyl orthosilicate, 99%), ammonium solution(25%), BTA (Benzotriazole, 99%), anhydrous ethanol, deionized water, APTES, hydrochloric acid. The following equipments were utilized in experiments from various sources. Enumerical-controlled ultrasonic cleaners of KQ22OOD model (Shanghai Book Training Experiment Equipment Co., Ltd), rotary evaporators (Gongyi City British Tongkuangyu instrument factory, Zhengzhou, China), Fourier transform infrared spectrometer (Beijing Rayleigh Analytical Instrument Company, Beijing, China), X-ray diffraction (XRD; PANalytical, Shanghai, China), UV-vis spectrophotometer (Agilent 8453,Shanghai industry mechanical and electrical equipment co., LTD), JSM-7500F model scanning electronic microscope (SEM, NEC Electronics Corporation), BOENI1400 model transmission Electron Microscope(TEM, Fairburn Industrial Development Co., Ltd., Shanghai), Energy Dispersive Spectroscopy(EDS, INCA), TG/DTA synchronization analyzer(SDTA851^e, Shanghai surplus promise Precision Instrument Co., Ltd.), BGD 750 blender (BIUGED Laboratory Instruments Equipment Limited Company, Guangzhou, China), ML204/02 electronic balance (Mettler Toledo Instruments Limited Company, Grefeinsee, Switzerland), YX-6050 model inhaled sandblasting machine (Yuxin Machinery Equipment Limited Company, Sichuan, China), and

electrochemical workstation (Shanghai Brilliance Instruments Limited Company, China).

2.2 Purification of HNTs

The purification of raw HNTs was carried out according to the method reported before[31]. Typically, raw HNTs (20g) were added into a mixture solution (200ml) containing 10 wt% of ethyl alcohol and 90 wt% of deionized water. Then 1 wt% of sodium hexametasphophate and 0.5-1 wt% of HCl were successively added into the suspension with the help of a magnetic stirring. The solution was stirred for 30 min, followed by standing for several days at room temperature. The clay impurities were precipitated in the bottom and removed by filtration. This operation was repeated several times until impurities were removed completely. The upper solution was carefully collected and the purified HNTs was separated by centrifugation, followed by drying at 60°C for 5 h. The purified HNTs (20–40nm×0.5–1.5μm (diameter×length)) are showed in figure 1.

2.3 Nanotube Loading Procedure

For the encapsulation of BTA, the HNTs (2g) were added into a solution of BTA in 40ml ethyl alcohol (80 mg/ml) and the suspension was treated via ultrasonic method for 20 min. The suspension was transferred to distillation flask of rotary evaporators, which was evacuated using a vacuum pump. When a slight fizzing came out from the suspension, the air in lumen of HNTs was being removed instead of BTA solution. After keeping under vacuum for 1h, the suspension was back to atmospheric pressure (Scheme 1, stage 1). To improve loading efficiency, this operation was repeated three

times[23].

2.4 Modification of HNTs and film formation

The above suspension was transferred to conical flask. Some deionized water (10 mL) and ammonium solution (0.5ml) were added into suspension, followed by dropwise addition of 0.5 mL TEOS. After stirring for 1 hour, the process of dropwise addition of TEOS was repeated once. Then the mixture was stirred by a magnetic stirring at a constant rotational speed for 10h. The formation of TEOS film were illustrated as follows:

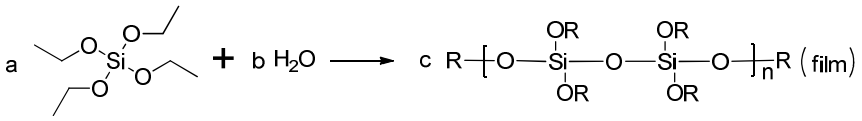

(1)

Subsequently, 0.5 mL APTES was added into above suspension (Scheme 1, stage 2), followed by stirring for 15 h at room temperature. A white emulsion was obtained after filtration, washing with pure water and drying at 60°C.

2.5 Characterization of nanocontainer

During preparation of the functional nanocontainer, some important derivatives as comparative specimens were synthesized in this paper, such as HNTs@TEOS and HNTs@TEOS-APTES hybrid material. To confirm the structure of HNTs@TEOS-APTES, some of test modes were utilized.

Information of chemical bonds on the surface of materials such as HNTs, HNTs@TEOS and HNTs@TEOS-APTES were obtained by Fourier transform infrared spectra. As for the X-ray diffraction patterns, the intensity of diffraction peaks and crystal form of samples were obtained and compared with each other. Afterwards, to analysis whether the APTES have grafted on the surface of film and

obtain the content of BTA loaded in nanocontainer, TG/DTA synchronization analyzer was utilized to test the thermal stability of the samples under N_2 atmosphere. The heating rate was 10°/min and the temperature range was between 25°C and 800°C, respectively. XPS method was utilized to visually confirm whether the HNTs have been successfully modified. In order to visually observe whether BTA has been loaded into nanotubes and TEOS has covered nanotubes, the TEM analysis of HNTs, BTA@HNTs, HNTs@TEOS and BTA@HNTs@TEOS-APTES were carried out. Afterwards, the dispersity of samples in ethyl alcohol and epoxy resin were measured by SEM and EDS, respectively. Nanocontainers were uniformly embedded in coating, which provides positive support for even dispersion of corrosion inhibitor in the coating.

2.6 BTA release kinetics

To understand the release rate of BTA from nanocontainer and assess a reasonable pH environment, UV-Vis spectroscopy was utilized. All release experiments were performed in deionized water (pH=1, 3, 5) at room temperature. The suspension (200ml) containing HNTs (0.2g) was constantly stirred in conical flask. In order to establish equilibrium conditions, continuous magnetic stirring was adopted during the release process. The BTA can gradually release from HNTs with the time increasing and the concentration of BTA in suspension was determined with absorbance of UV-Vis spectroscopy at 260 and 273nm wavelength. Meanwhile, it is also utilized to assure whether BTA have been loaded in the lumen of HNTs by the formation of TEOS film.

2.7 Electrochemical and scarification experiment

Anticorrosion coating was prepared by dispersing 3 wt% of synthesized nanocontainers (BTA@HNTs@TEOS-APTES) into epoxy resin. Afterwards, the nanocontainers were added into epoxy resin via stirring and ultrasonic treatment for 20 min by numerically controlled ultrasonic cleaners KQ22OOD model. Before the steel specimens were immersed into the corrosive medium, the steel specimens surface were abraded successively with different grades of emery paper (grade 240, 360, 800). Then, the specimens were degreased with acetone, washed with ethanol and thoroughly dried. Next, to guarantee the correctness and consistency of experimental data, the steel specimens were coated by the anticorrosion coating with thickness (tested by coating thickness gauge QNix4500 model) of 120-150μm. Electrochemical impedance spectroscopy (EIS) measurements were employed to determine the anticorrosion performance of the coatings with different immersing time. Soaking experiments were used to assess the durability of anticorrosion performance of coatings in the aggressive solution (3.5% NaCl, pH=3). The coatings were used to test the anticorrosion ability of corrosion inhibitor releasing from coating with cross scratches which were done manually by razor blade. Subsequently, optical photography was used to assess the corrosion performance of the coatings. The coating (BTA@HNTs@TEOS-APTES/epoxy) with corrosion inhibitor and without were immersed in corrosion medium (10% NaCl, pH=3) after 24h of immersion.

3. Results and discussion

3.1 FT-IR analysis of samples

Commonly, core-shell structures are prepared based on a template-assisted approach in which the core particle is coated by shells with different materials. However, this method often needs surface functionalization of the nanoparticle to grow the shells around the cores[32]. Several reports confirmed that HNTs contains many groups which also locate between layers and bound of nanotubes. As shown in figure 2a, HNTs have various functional groups, such as two stretching absorptions of Al_2OH(3695cm^{-1}, 3621 cm^{-1}), Al-OH bending absorbs(905 cm^{-1}), an absorption peak of O-Si-O, O-H deformation of water absorptions and another, which can take effective help to assemble the structure of HNTs@TEOS. To ascertain the structure of samples, the FT-IR analysis of HNTs, HNTs@TEOS and HNTs@TEOS-APTES was carried out between 400 and 4400 cm^{-1}. By comparison of the FT-IR curves(a, b), it can be clearly seen that a new peak around 1383 cm^{-1} is assigned to C-H deformation absorption of TEOS film. For the curve (c) of modified nanocontainer, the stretching absorption of primary amino (double peaks) from addition of APTES appear at 3414 cm^{-1} and 3477 cm^{-1}. Therefore, based on the above analysis, we can infer that TEOS film and APTES has been successfully coated on the surface of HNTs.

3.2 X-ray diffraction analysis of samples

The XRD patterns revealed the diffraction peaks of the HNTs, HNTs@TEOS, HNTs@TEOS-APTES. The characteristic diffraction peaks at 2θ=12.17°, 20.11°, 24.69°, 35.10°, 38.46°, 54.69°, 62.45°, 73.75° and 77.09° are assigned to pure HNTs component according to standard JCPDS card no.29-1487 (Figure 3a). Compare to the Figure 3a, the abscissas of the diffraction peaks for two curves (Figure 3b,c)

almost not change, which suggests that the crystalline form of HNTs was not altered after addition of TEOS and APTES. However, the intensity of diffraction peaks in Figure 3b and 3c turns weaker successively. This is due to the fact that shielding layer of TEOS film and modification of organic material (APTES) covered the surface of HNTs[33].

3.3 TGA analysis of samples

To further study the BTA loaded in lumen of HNTs, TGA was employed to obtain the content of encapsulated BTA. Meanwhile, the DTG can confirm the grafting of APTES on the surface of TEOS film. Figure 4 illustrates the TGA curves of the obtained BTA@HNTs@TEOS-APTES, HNTs@TEOS, HNTs@TEOS-APTES and pure HNTs powders. The weight percentage of BTA encapsulated in nanotubes can be estimated from the TGA curves. It is clearly observed that the curves declined at 450-550°C. Hence, the weight loss of BTA@HNTs@TEOS-APTES at 50-300°C was attributed to the decomposition of BTA and the dehydration of the powder. As it revealed in the TGA curve of figure 4a, the 0.75% weight loss of BTA@HNTs@TEOS-APTES at 50-120°C corresponded to the dehydration of BTA@HNTs@TEOS-APTES. About 22.6% weight loss of BTA@HNTs@TEOS-APTES at 120-300 °C was observed, which was corresponded to the decomposition of BTA. Thus, the weight percentage of BTA in BTA@HNTs@TEOS-APTES was about 22.6 %. Figure 5 shows the derivative thermogravimetry of APTES, HNTs@TEOS and HNTs@TEOS-APTES. As can be seen that the maximum decomposition rate of APTES is 268°C. However, the

modified powders (HNTs@TEOS-APTES) and powders without modification (HNTs@TEOS) are not degraded at 268℃, indicating that no free state of APTES was adsorbed on the surface of TEOS film and APTES were grafted on the surface of TEOS film via chemical bond[34].

3.4 XPS analysis of samples

The surface compositions of nanocontainers (HNTs@TEOS, HNTs@TEOS-APTES) were investigated by XPS analysis and the results are shown in Table 1. Figure 6 shows the high-resolution XPS spectra of O 1s and N 1s region of the prepared nanocontainers. The O 1s spectrum of HNTs@TEOS and HNTs@TEOS-APTES are curve-fitted with two peak components for Si-O-Si and Al-O-H species at the binding energies of about 532.6 and 531.7eV, respectively (figure 6a,b)[35-37]. The surface elemental mole percentage of Al in nanocontainer(HNTs@TEOS) decreased from 9.4 to 3.18 at% compared with the modified nanocontainer(HNTs@TEOS-APTES). This is caused by surface modification via addition of APTES. Similarly, the peak area percentage of Al-O-H decreased from 62.15 to 34.74 at%. On the contrary, the peak area percentage of Si-O-Si is about 78.86 at% for the modified nanocontainer, which is higher than that of the HNTs@TEOS (67.13 at%). It demonstrated that the new chemical bond of Si-O-Si formed between APTES and HNTs@TEOS. These results confirmed that the APTES was successfully grafted on the surface of HNTs@TEOS. In addition, as shown in Figure 6c, The N 1s spectrum of HNTs@TEOS-APTES is curve-fitted with two peak components for $–NH_2$ and $-NH_2$/-NH-/NH_3^+ species, at the binding energies

of about 399.4eV and 401.5eV, respectively[38]. The result suggested that there are some primary amino on the surface of HNTs@TEOS-APTES which is in agreement with FTIR result.

3.5 TEM analysis of samples

In order to visually observe whether BTA and nanotubes were encapsulated via nanocontainer and TEOS. TEM analysis of pure HNTs, BTA@HNTs, HNTs@TEOS and BTA@HNTs@TEOS-APTES particles were carried out, as shown in Figure 7. As seen in the images of pure HNTs (Figure 7a) and BTA@HNTs (Figure 7b), the inner space of halloysite filled with BTA is obvious. Meanwhile, the smooth surface of BTA@HNTs indicates that BTA did not cover the surface of BTA@HNT. As shown in Figure 7c, the HNTs were clearly coated by smooth TEOS film. While, for the modified nanocontainer (Figure 7d), the morphology showed quite different from BTA@HNTs (Figure 7b) and HNTs@TEOS (Figure 7c). It can be seen that halloysite was completely covered by organic matter on the surface of TEOS film after modification, indicating that halloysite has successfully been modified. This observation is well agreement with the results of FT-IR, XRD, TGA and XPS. Based on these discussion, the structure of BTA@HNTs@TEOS-APTES have been successfully assembled.

3.6 Controlling release rates with pH value

In the aggressive media, the release rate of BTA is required at a reasonable speed, which directly impacts the anticorrosion performance of functional coating in long-term period. Low level of release rate for BTA will not contribute to the corrosion resistance of coating. On the contrary, as the release rate increased, large

amounts of corrosion inhibitor exposes out of container. The result cause corrosion inhibitor to be out of function at soon in corrosion medium. Thus, it can be speculated that the release rate is significant for anti-corrosion process in long-term. To better understand and assess release process of BTA from container, the UV-vis spectroscopy was employed to observe the variation of release rate from absorbance. As it is shown in figure 8b, since the pH value of solution was adjusted to be 3 with hydrochloric acid, the absorbance of BTA gradually increased with increase of time. However, in figure 8a, the absorbance sharply augments after the pH value of solution was adjusted to be 1. But, the absorbance changed little after 30 min of releasing. As can be seem from the figure 8c that the absorbance was almost no change all the time even the pH value of solution was adjusted to be 5. Similarly, corresponding releasing rate of BTA in figure 8d visually describes these three phenomenon which are related to the rate of reaction between hydrogen ions and silicon ether. Decomposition of the TEOS film takes place according to the following reaction:

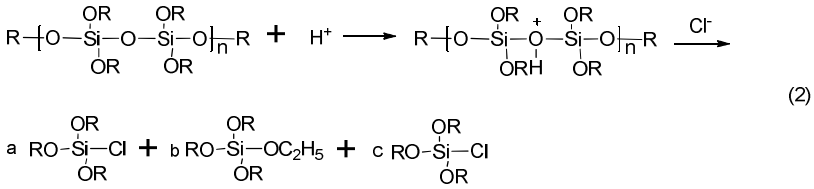

(2)

The switch of the BTA release based on the above reaction is demonstrated. With the concentration of hydrogen ions increasing, the degradation rate of film increased, which led to the increase of release rate. Hydrogen ions is regarded as a key to the door (TEOS film). Its concentration determines the size of a crack between a door and its frame, which vividly illustrates the smart function for the release process of BTA.

3.7 Dispersity of nanocontainer

Since HNTs was discovered firstly, it has been extensively investigated in anticorrosion performance of electroplated coating[28] and organic coating[39, 40]. Although HNTs have many superior properties, they also cannot be uniformly dispersed in aqueous/organic solvents attributing to the strong intertube van der Waals force attraction. The introduction of the outer TEOS film not only encapsulated the corrosion inhibitor, but also provided reaction sites for further functionalization with amine groups by APTES[41], which can improve dispersibility of nanocontainers in epoxy resin[42]. Thus, with the purpose of inspecting the dispersion of HNTs in ethyl alcohol and epoxy resin, the HNTs and anticorrosion coating prepared with dispersed nanocontainers were investigated by SEM and EDS. Figure 9 (A, B, C) depicts the different nanomaterials(HNTs, HNTs@TEOS, BTA@HNTs@TEOS-APTES) dispersed in ethyl alcohol. It can be concluded that the dispersity of nanocontainer(BTA@HNTs@TEOS-APTES) have been improved. Further test was applied in epoxy resin. Figure 10 depicts the cross section of the coating and corresponding Si and N mapping of composite coating. As shown in image (figure 10a), there were no agglomerates of particles on the surface of cross section of composite coating. Figure 10b and c describe the Si and N elements uniformly distributing in the epoxy matrix, respectively. This observation demonstrated that nanocontainers (BTA@HNTs@TEOS-APTES) were well dispersed in pure epoxy resin and provided a strong support for the good corrosion resistance of coating.

3.8 Anticorrosion performance of coating

Furthermore, in order to better understand the coating corrosion resistance, EIS was

employed to assess the corrosion protection performance of the coating with inhibitor-loaded HNTs nanocontainers. Figure 11(a, b) shows the Bode plots of the coating loaded with corrosion inhibitor (BTA) after immersing of 12, 24, 48, 72, 102, 132, 162, 192 h and pure epoxy coating after immersing of 12h in 3.5 wt% NaCl acidic solution(pH=3). As it can be seen from the Figure 11a, with the increase of immersion time, an interesting phenomenon can be achieved from the low frequency impedance (0.01-0.1 Hz). With the increase of immersion time, some of the low-frequency impedance resistance of functional coating is larger than former. As the immersion time is up to 72 h, the impedance raises remarkably. After immersing of 72 h, the low-frequency impedance resistance starts to decrease. In spite of appearing a decrease trend, the falling speed for impedance resistance is less. Meanwhile, the impedance of coating (BTA@HNTs@TEOS-APTES/epoxy) at time of 192 hours is also higher than that of pure epoxy coating at time of 12 hours. The values of the low-frequency impedance could be treated as an important factor to evaluate the anticorrosion performance of coating. Figure 11b is about phase angle changing with the frequency varying and shows two well-defined time constants in curves. The time constant at high frequencies (1-100 Hz) is attributed to the coating response. The second time constant observed in the low frequencies (0.01-0.1Hz) is related to the presence of the intermediate film layer. But, two time constants appearing in the curve of pure epoxy coating were different from other curves. It is worth mentioning that both of the two time constants in the curve of pure epoxy coating appear at high frequencies (1-100 Hz). So, it can indicate that the corrosion medium has passed

through pure epoxy coatings from micropores and arrived at substrate[34, 43]. Therefore, the pure epoxy coating has lost the anti-corrosion ability after 12 h of immersion and the duration of the sample is at least 16 times as high as that of the pure epoxy coating. For the spectra of functional coating in Figure 11b, the phase angle at the high frequency time presents a decrease trend with the time increasing, indicating that the functional coating was gradually lost for protection against metal. In contrast, a growing trend can be observed at the low frequency, suggesting the impedance of intermediate film layer gradually strengthened. Although there is an opposite tendency of corrosion protection, the functional coating can keep stable state for a long immersion time and show a high corrosion resistance performance. As shown in the Fig.12, the surface morphology of the coatings is tested by the SEM images after immersing for 80 days. The corresponding surface of the pure epoxy coating involved some corrosion products, cracks and peeling phenomenon (figure 12a). But, the corroded surface of composite coating displays smooth and uniform (figure 12b). To confirm the existence of above opposite tendency and obtain a better understanding about the corrosion behavior of functional coating, the impedance spectra was fitted using the equivalent circuit by ZSimpWin version software as shown in Figure 13 and the simulating data was listed in Table 2. The equivalent circuit consists of the following elements: R_{sol} is the electrolyte resistance; R_{coat} is the coating resistancce; Q_{coat} represents constant phase angle element (CPE) for coating; R_{film} and C_{film} are the resistance and capacitance of the intermediate film layer. Table 2 shows the value of R_{coat} gradually decreased from the initial value of 11170 to

6132Ωcm^2 after 192h of immersion, while the initial value of resistance of the intermediate film layer ($R_{film)}$ increased between 24h and 102h. As the time of immersion proceeded, R_{film} reached a maximum value (1893) after 102h of immersion, indicating that corrosion inhibitor gradually releasing from nanocontainer played a very important role in the protection of metal. After 102h of immersion, R_{film} constantly decreased during the remaining time, suggesting that the effect of corrosion inhibitor began to weaken. Although the coating was not very effective for resisting the invasion of corrosive medium, the corrosion inhibitor as reinforcing means could play a vital role in the metal protection in the long-term.

3.9 Scarification test

Scarification test can visually understand and assess the anticorrosion performance of corrosion inhibitor releasing from nanocontainer. The nanocontainers (loaded with corrosion inhibitor and without corrosion inhibitor) were dispersed into the pure epoxy resin with the nanocontainers of 3wt%. Before the steel specimens sprayed with functional coating were immersed in 10 wt% NaCl solution (pH=3), cross scratches were applied manually on the coating by razor blade. It can be seen from the figure 14a and 14b, the scratches of steel specimen with the nanocontainers loading with corrosion inhibitor (BTA@HNTs@TEOS-APTES/epoxy) and without (HNTs@TEOS-APTES/epoxy) is smooth. After immersing of 24h, there is a distinct difference between the two specimens. The scarification of coating specimen (figure 14a) is still smooth and no color products is in it. In contrast, for the coating specimen (figure 14b), reddish brown products were formed in the scratches. This result clearly

demonstrates that the anticorrosion performance of coating (BTA@HNTs@TEOS-APTES/epoxy) was better than that of coating (HNTs@TEOS-APTES/epoxy) when the coatings were damaged by external mechanical forces. Meanwhile, this test provided an indirect evidence that release of corrosion inhibitor played a key role for protecting substrate in acid corrosive medium. The released corrosion inhibitor as a film attached on the sheet steel in the damaged area and ensured a long-term anticorrosion of coating. The mechanism of BTA protecting behavior was shown in scheme 2.

4. Conclusion

HNTs containing corrosion inhibitors offered essential benefits to epoxy coatings. The structure of nanocontainer was assembled successfully through a facile approach, which was characterized by FT-IR, XRD and TEM. The content of corrosion inhibitor encapsulated into nanocontainer was about 22.6wt%, as confirmed by TGA. The releasing rate of BTA was controlled by pH value and monitored via UV-vis, which achieves an optimal pH value (pH=3). The modified nanocontainer can be well dispersed in ethyl alcohol and epoxy resin, which infers that corrosion inhibitor releasing from nanocontainer could evenly disperse in the epoxy resin. Corrosion protection performance of the coating was evaluated by EIS method, which showed that the anticorrosion coating loaded with corrosion inhibitor could provide a long-term protection against metal corrosion in the aggressive medium (3.5wt% NaCl, pH=3). Scarification test visually displayed the mechanism of corrosion protection behavior of the encapsulated corrosion inhibitor in corrosive medium (10wt% NaCl,

pH=3).

References

[1] Y. Liu, D. Sun, H. You, J.S. Chung, Applied Surface Science, 246 (2005) 82-89.
[2] W.S. G. Grundmeier, M. Stratmann, Electrochimica Acta, 45 (2000) 2515-2533.
[3] D. Raps, T. Hack, J. Wehr, M.L. Zheludkevich, A.C. Bastos, M.G.S. Ferreira, O. Nuyken, Corrosion Science, 51 (2009) 1012-1021.
[4] P.Q. R. Ramanauskas, L. Maldonado, R. Pomes, M.A. Pech-Canul, Surface and Coatings Technology, 92 (1997) 16-21
[5] Y.S. Huang, X.T. Zeng, X.F. Hu, F.M. Liu, Electrochimica Acta, 49 (2004) 4313-4319.
[6] M.R. Vaezi, S.K. Sadrnezhaad, L. Nikzad, Colloids and Surfaces A: Physicochemical and Engineering Aspects, 315 (2008) 176-182.
[7] E.S. Ferreira, C. Giacomelli, F.C. Giacomelli, A. Spinelli, Materials Chemistry and Physics, 83 (2004) 129-134.
[8] M. Elayyachy, A. El Idrissi, B. Hammouti, Corrosion Science, 48 (2006) 2470-2479.
[9] F.G. G. Moretti, Corrosion Science, 44 (2002) 1995-2011.
[10] U. Yoshihiko, Takayuki, Kitamura, Ryuichi Ohtani, Composites Science and Technology 53 (1995) 333-341.
[11] L. Huang, N. Yi, Y. Wu, Y. Zhang, Q. Zhang, Y. Huang, Y. Ma, Y. Chen, Advanced materials, 25 (2013) 2224-2228.
[12] F. Zhang, L. Zhao, H. Chen, S. Xu, D.G. Evans, X. Duan, Angewandte Chemie, 47 (2008) 2466-2469.
[13] H.F. Guo, M.Z. An, Applied Surface Science, 246 (2005) 229-238.
[14] D. Li, F. Wang, X. Yu, J. Wang, Q. Liu, P. Yang, Y. He, Y. Wang, M. Zhang, Progress in Organic Coatings, 71 (2011) 302-309.
[15] M. Behzadnasab, S.M. Mirabedini, K. Kabiri, S. Jamali, Corrosion Science, 53 (2011) 89-98.
[16] M. Quinet, B. Neveu, V. Moutarlier, P. Audebert, L. Ricq, Progress in Organic Coatings, 58 (2007) 46-53.
[17] A.N. Khramov, N.N. Voevodin, V.N. Balbyshev, M.S. Donley, Thin Solid Films, 447-448 (2004) 549-557.
[18] Y.J.L. Cao P G, Zheng J W, Langmuir, 18 (2002) 100-104.
[19] G. Bereket, A. Pinarbaşi, Corrosion Engineering, Science and Technology, 39 (2004) 308-312.
[20] K. Babić-Samardžija, N. Hackerman, Journal of Solid State Electrochemistry, 9 (2005) 483-497.
[21] E. Abdullayev, V. Abbasov, A. Tursunbayeva, V. Portnov, H. Ibrahimov, G. Mukhtarova, Y. Lvov, ACS applied materials & interfaces, 5 (2013) 4464-4471.
[22] D. Fix, D.V. Andreeva, Y.M. Lvov, D.G. Shchukin, H. Möhwald, Advanced Functional Materials, 19 (2009) 1720-1727.
[23] E. Abdullayev, R. Price, D. Shchukin, Y. Lvov, ACS applied materials & interfaces, 1 (2009) 1437-1443.
[24] P.B.D. S.R. Levis, International Journal of Pharmaceutics, 243 (2002) 125-134.
[25] D.G. Shchukin, G.B. Sukhorukov, R.R. Price, Y.M. Lvov, Small, 1 (2005) 510-513.
[26] A.J.M. John L. Keeling, Keith M. Scott, Kerri Hartley, Advances in Regolith, (2003) 230-233.
[27] Z. Luo, H. Song, X. Feng, M. Run, H. Cui, L. Wu, J. Gao, Z. Wang, Langmuir, 29 (2013) 12358-12366.
[28] S. Ranganatha, T.V. Venkatesha, K. Vathsala, Applied Surface Science, 263 (2012) 149-156.

[29] M.-J. Jiang, Z.-M. Dang, S.-H. Yao, J. Bai, Chemical Physics Letters, 457 (2008) 352-356.
[30] N. Yan, J.K. Wu, Y.H. Zhan, H.S. Xia, Plastics, Rubber and Composites, 38 (2009) 290-296.
[31] M. Liu, B. Guo, M. Du, Y. Lei, D. Jia, Journal of Polymer Research, 15 (2007) 205-212.
[32] X.D. Wu X J, Journal of the American Chemical Society, 131 (2009) 2774-2775.
[33] Y. He, C. Chen, F. Zhong, H. Chen, D. Qing, Polymers for Advanced Technologies, 26 (2015) 414-421.
[34] Y. He, Y. Fan, C. Chen, F. Zhong, D. Qing, High Performance Polymers, 27 (2014) 191-199.
[35] F.C.S. Alvarez R, Silva J A, Soil Science Society of America Journal, 40 (1976) 615-617.
[36] J.T. Kloprogge, L.V. Duong, B.J. Wood, R.L. Frost, Journal of colloid and interface science, 296 (2006) 572-576.
[37] J. Serra, P. González, S. Liste, C. Serra, S. Chiussi, B. León, M. Pérez-Amor, H.O. Ylänen, M. Hupa, Journal of Non-Crystalline Solids, 332 (2003) 20-27.
[38] L. Zhang, Q. Jin, J. Huang, Y. Liu, L. Shan, X. Wang, Applied Surface Science, 256 (2010) 5911-5917.
[39] D.G. Shchukin, D.O. Grigoriev, H. Möhwald, Soft Matter, 6 (2010) 720.
[40] S. Dmitry G, S. V. Lamaka,. A. Yasakau,M. L. Zheludkevich, M. G. S. Ferreira, H. Mohwald, J. Phys. Chem, 112 (2008) 958-964.
[41] Y. Lu, B. He, J. Shen, J. Li, W. Yang, M. Yin, Nanoscale, 7 (2015) 1606-1609.
[42] W. Sassi, L. Dhouibi, P. Berçot, M. Rezrazi, E. Triki, Electrochimica Acta, 117 (2014) 443-452.
[43] F. Zucchi, V. Grassi, A. Frignani, G. Trabanelli, Corrosion Science, 46 (2004) 2853-2865.

Figure 1. SEM images of purified HNTs

Scheme 1. Assemble procedure of functional nanocontainer (BTA@HNTs@TEOS-APTES)

Figure 2. The FT-IR spectrum of nanotubes

Figure 3. X-ray diffraction spectra of nanotubes

Figure 4. The thermal degradation map of nanotubes

Figure 5. Derivative thermogravimetry of nanotubes

Figure 6. X-ray Photoelectron Spectroscopy of nanotubes(HNTs@TEOS, HNTs@TEOS-APTES)

Figure 7. Transmission electron microscope of nanotubes

Figure 8. UV-vis spectroscopy(a-c) of BTA@HNTs@TEOS-APTES(1g/L) in different pH value (1,3,5) of water solution and corresponding releasing rate of BTA

Figure 9. A, B, C are the SEM images of different nanomaterials(HNTs, HNTs@TEOS, BTA@HNTs@TEOS-APTES) dispersed in ethyl alcohol

Figure 10. Typical SEM images of cross-section and corresponding Si and N mapping of BTA@HNTs@TEOS-APTES/epoxy

Figure 11. The Bode plots of the coating loaded with corrosion inhibitor (BTA) at different time

Figure 12. The SEM images of pure epoxy and composite coating (BTA@HNTs@TEOS-APTES/epoxy) after immersing for 80 days

Figure 13. Equivalent circuit for the composite(BTA@HNTs@TEOS-APTES/epoxy)

Figure 14. Scarification test for BTA@HNTs@TEOS-APTES/epoxy(a) and

HNTs@TEOS-APTES/epoxy(b) in 10 wt% NaCl solution (pH=3); after immersing for 24h, the results for counter specimens a' and b'

Scheme 2. The working mechanism of nanocontainer-based coatings

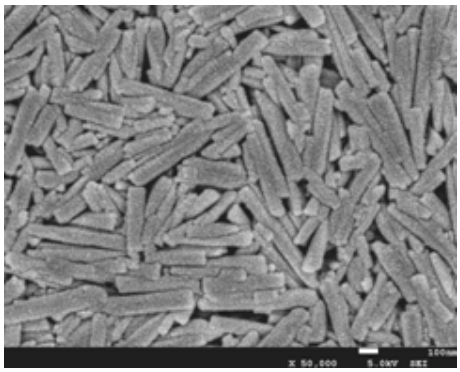

Figure 1

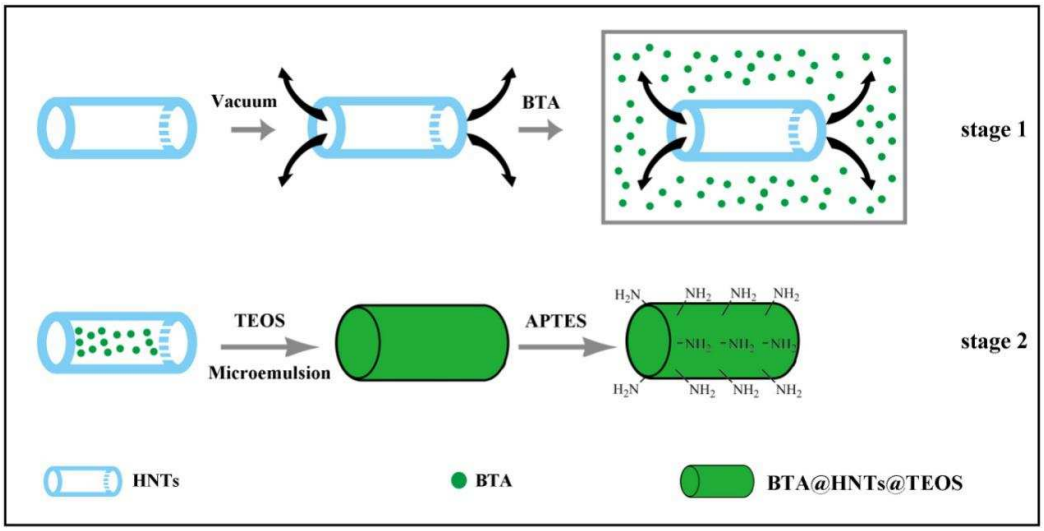
Vacuum
BTA
stage 1
TEOS
Microemulsion
APTES
stage 2
HNTs
BTA
BTA@HNTs@TEOS

Scheme 1

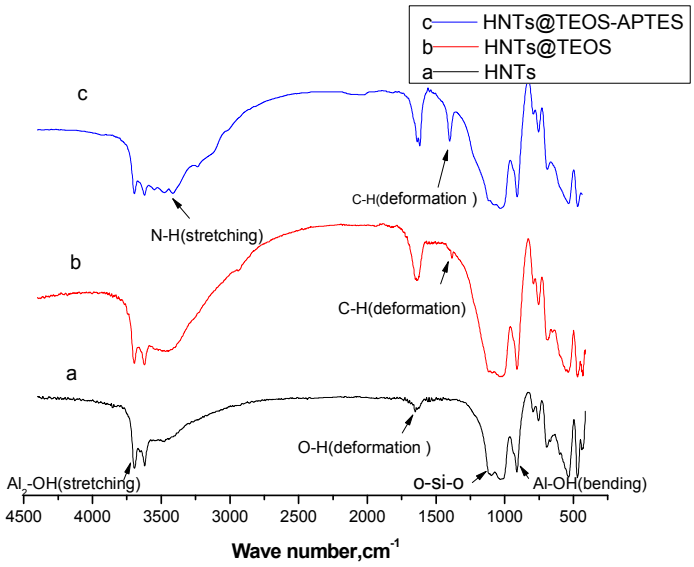
c HNTs@TEOS-APTES
b HNTs@TEOS
a HNTs
c
N-H(stretching)
C-H(deformation)
b
C-H(deformation)
a
O-H(deformation)
Al-OH(stretching)
Si-O
Al-OH(bending)
4500 4000 3500 3000 2500 2000 1500 1000 500
Wave number,cm-1

Figure 2

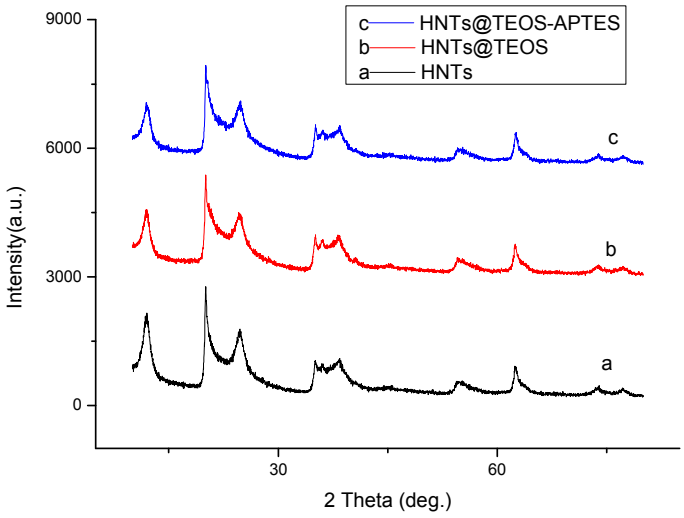
c HNTs@TEOS-APTES
b HNTs@TEOS
a HNTs
9000
6000
3000
0
Intensity(a.u.)
30
60
2 Theta (deg.)
c
b
a

Figure 3

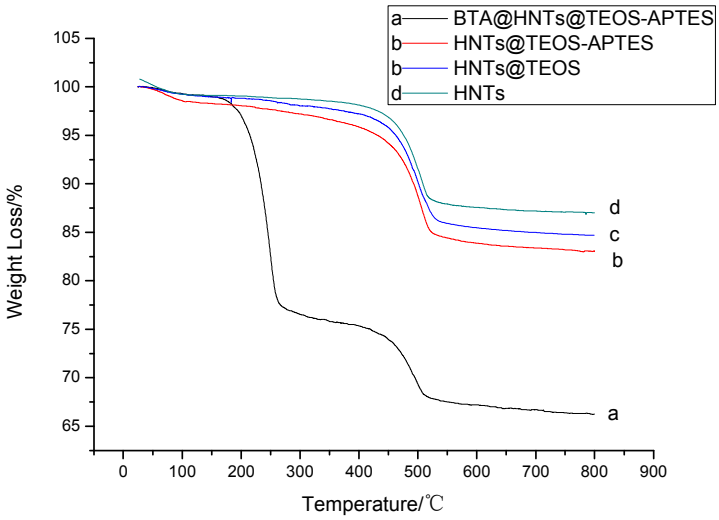
a BTA@HNTs@TEOS-APTES
b HNTs@TEOS-APTES
b HNTs@TEOS
d HNTs
Weight Loss/%
Temperature/℃
105
100
95
90
85
80
75
70
65
0
100
200
300
400
500
600
700
800
900
d
c
b
a

Figure 4

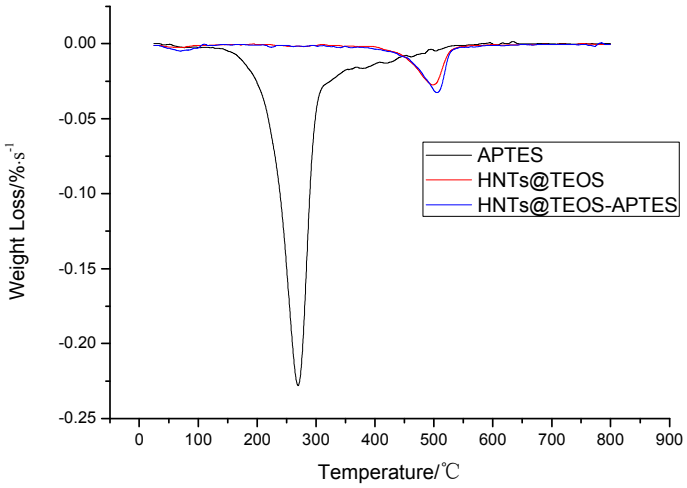
0.00
-0.05
-0.10
-0.15
-0.20
-0.25
Weight Loss/%·s-1
0
100
200
300
400
500
600
700
800
900
Temperature/℃
APTES
HNTs@TEOS
HNTs@TEOS-APTES

Figure 5

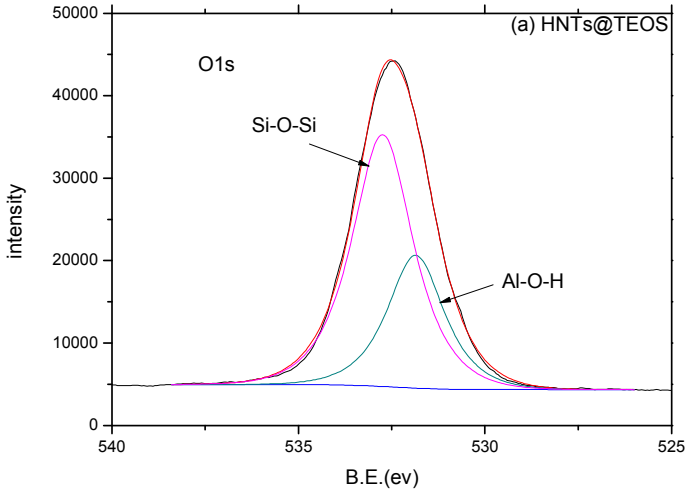
(a) HNTs@TEOS
O1s
Si-O-Si
Al-O-H
intensity
B.E.(ev)
50000
40000
30000
20000
10000
0
540
535
530
525

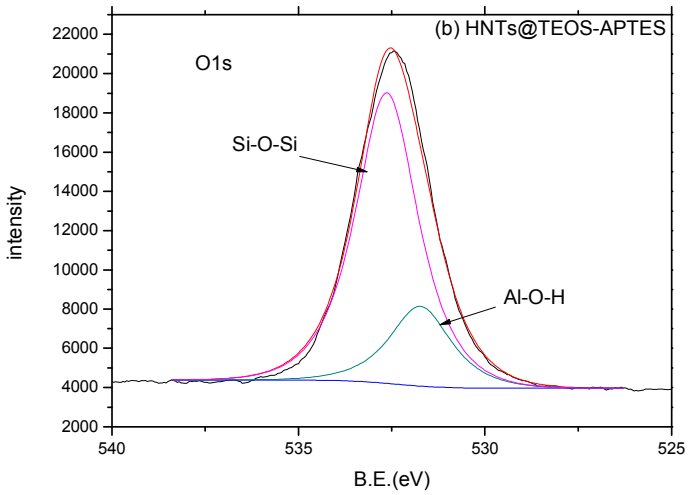
(b) HNTs@TEOS-APTES
O1s
Si-O-Si
Al-O-H
intensity
B.E.(eV)
22000
20000
18000
16000
14000
12000
10000
8000
6000
4000
2000
540
535
530
525

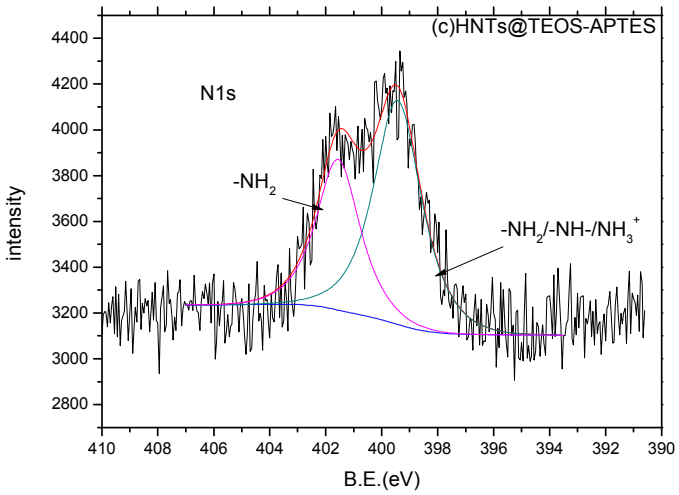
(c)HNTs@TEOS-APTES
N1s
-NH2
-NH2/-NH-/NH3+
intensity
B.E.(eV)
4400
4200
4000
3800
3600
3400
3200
3000
2800
410
408
406
404
402
400
398
396
394
392
390

Figure 6

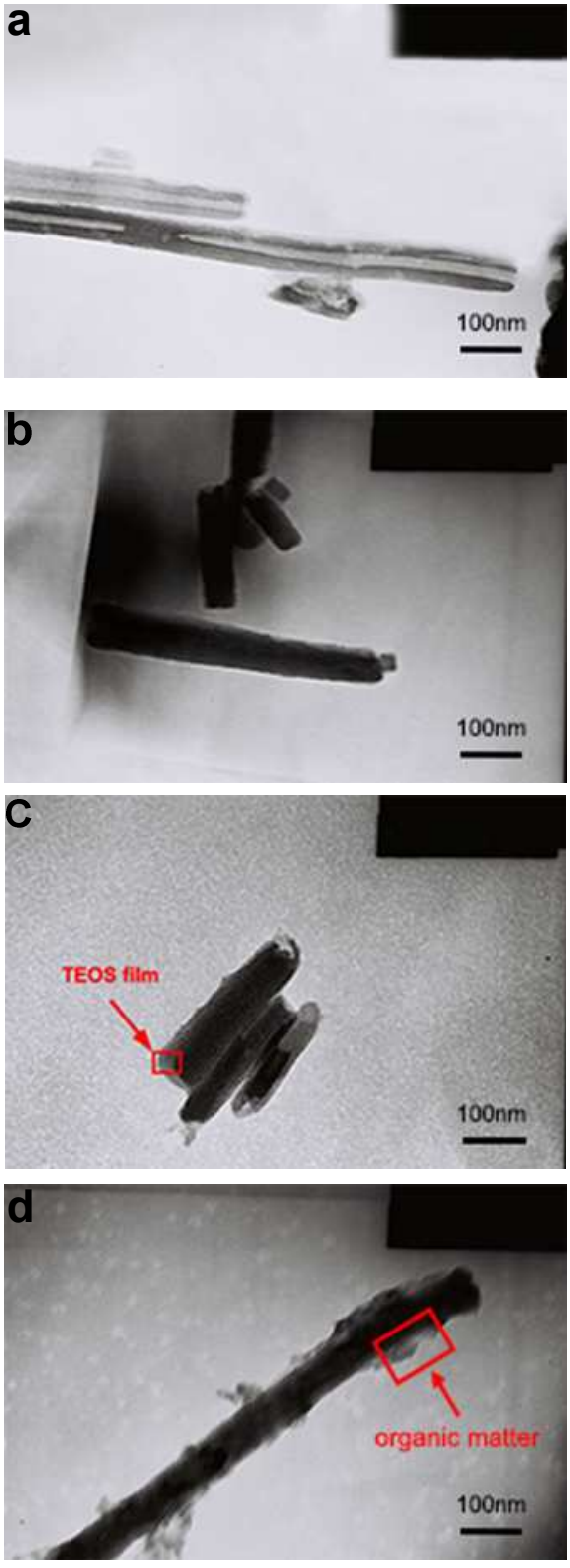

Figure 7

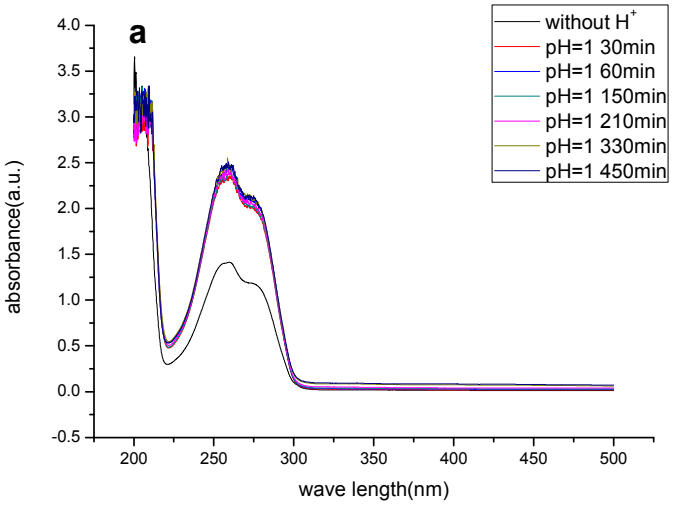
a
without H+
pH=1 30min
pH=1 60min
pH=1 150min
pH=1 210min
pH=1 330min
pH=1 450min
absorbance(a.u.)
wave length(nm)

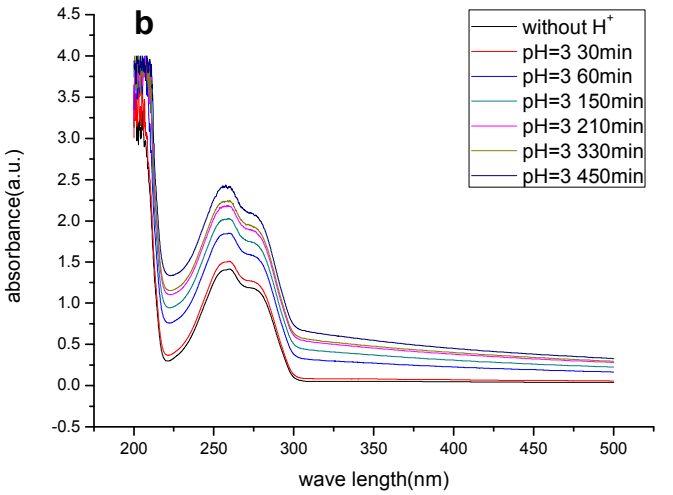
b
without H+
pH=3 30min
pH=3 60min
pH=3 150min
pH=3 210min
pH=3 330min
pH=3 450min
absorbance(a.u.)
wave length(nm)

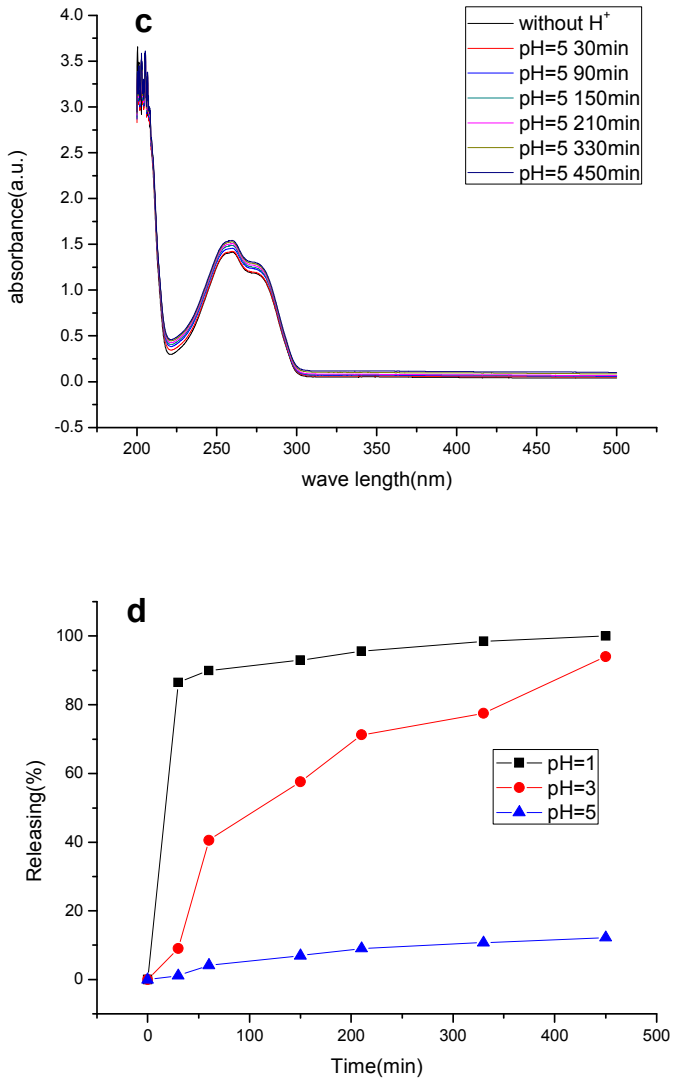
c
without H+
pH=5 30min
pH=5 90min
pH=5 150min
pH=5 210min
pH=5 330min
pH=5 450min
absorbance(a.u.)
wave length(nm)
d
pH=1
pH=3
pH=5
Releasing(%)
Time(min)

Figure 8

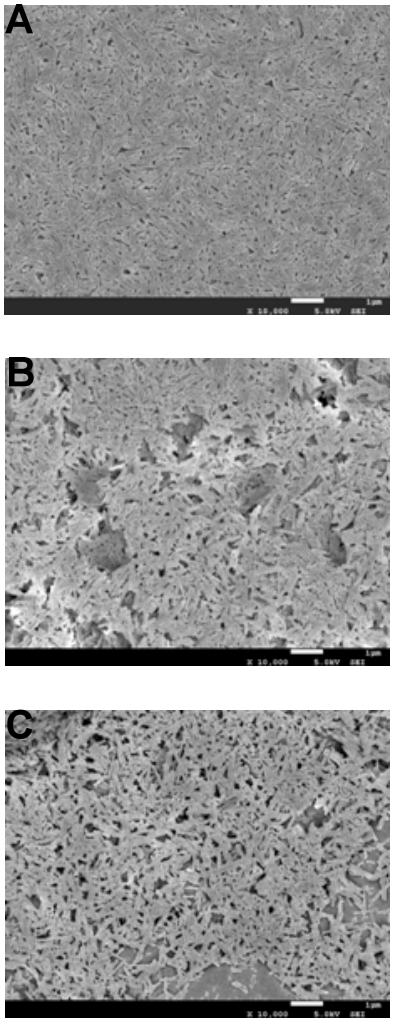

Figure 9

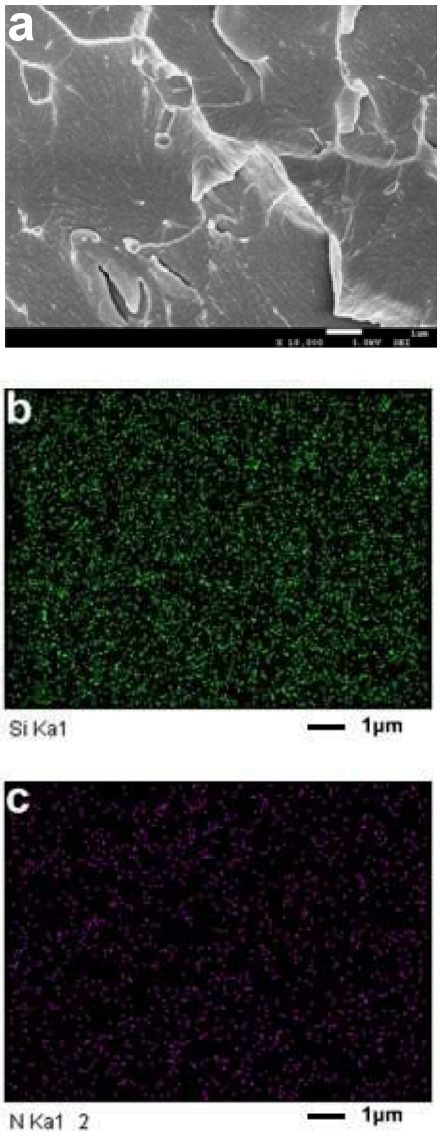

Figure 10

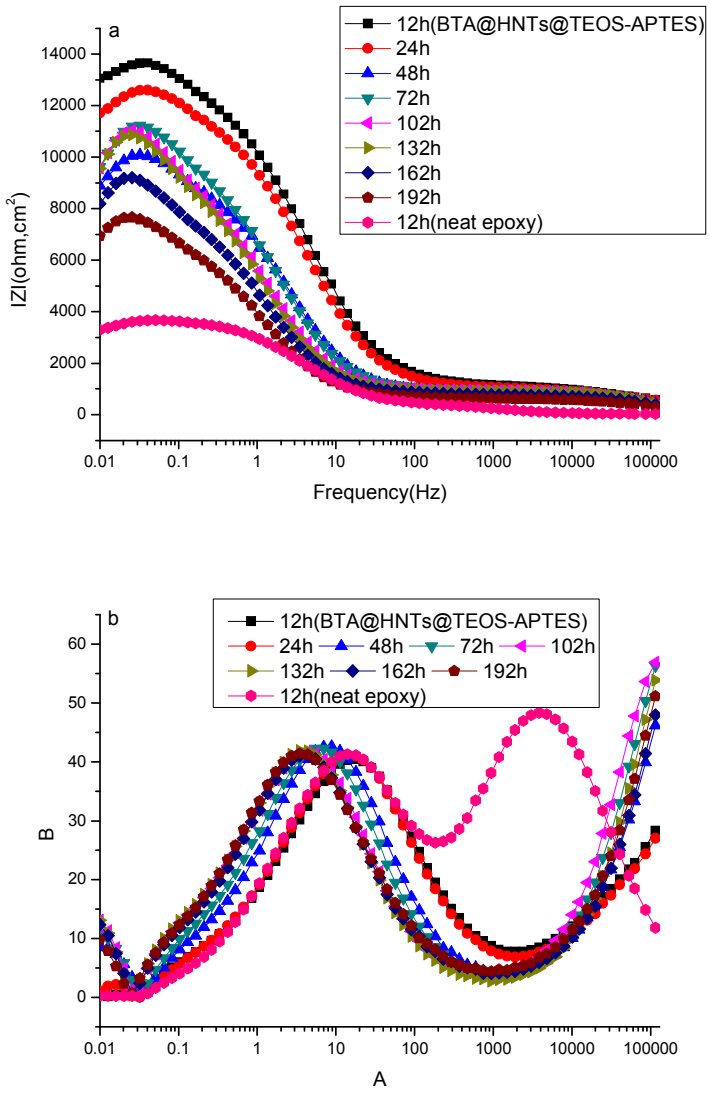
a
12h(BTA@HNTs@TEOS-APTES)
24h
48h
72h
102h
132h
162h
192h
12h(neat epoxy)
|Z|(ohm,cm^2)
Frequency(Hz)
b
12h(BTA@HNTs@TEOS-APTES)
24h
48h
72h
102h
132h
162h
192h
12h(neat epoxy)
B
A

Figure 11

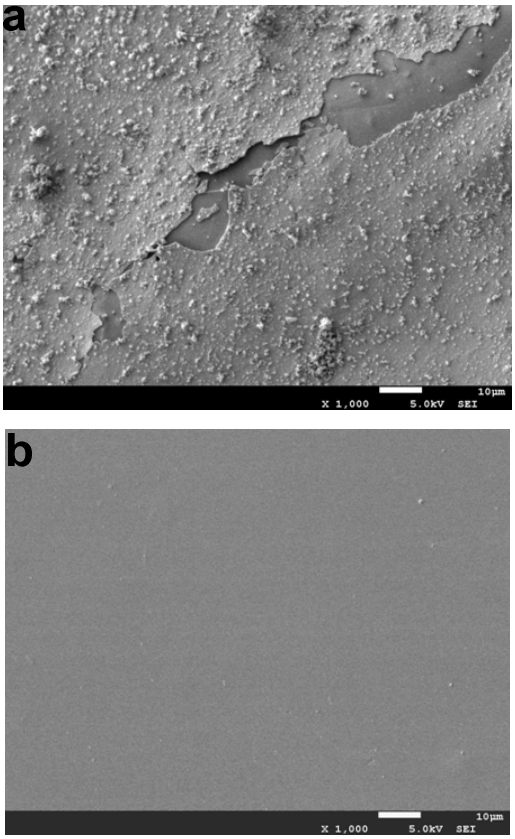

Figure 12

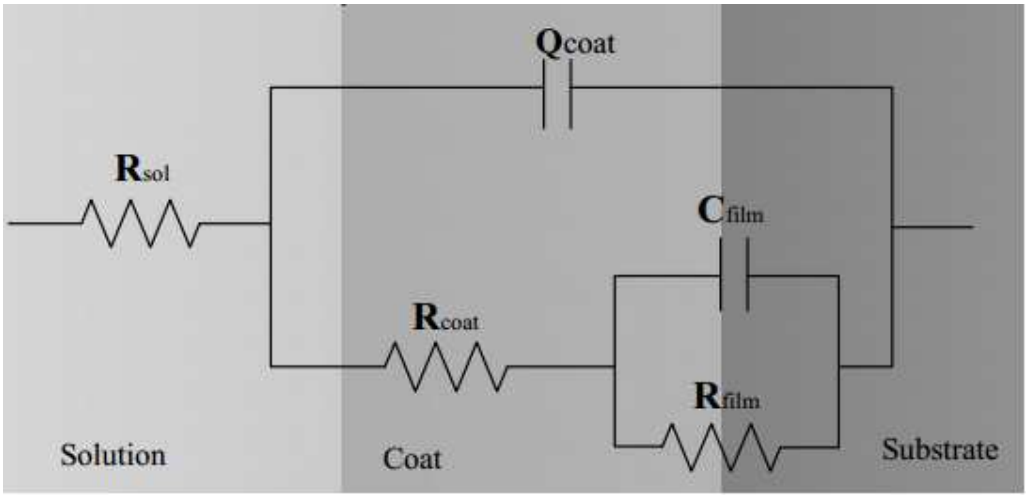

Figure 13

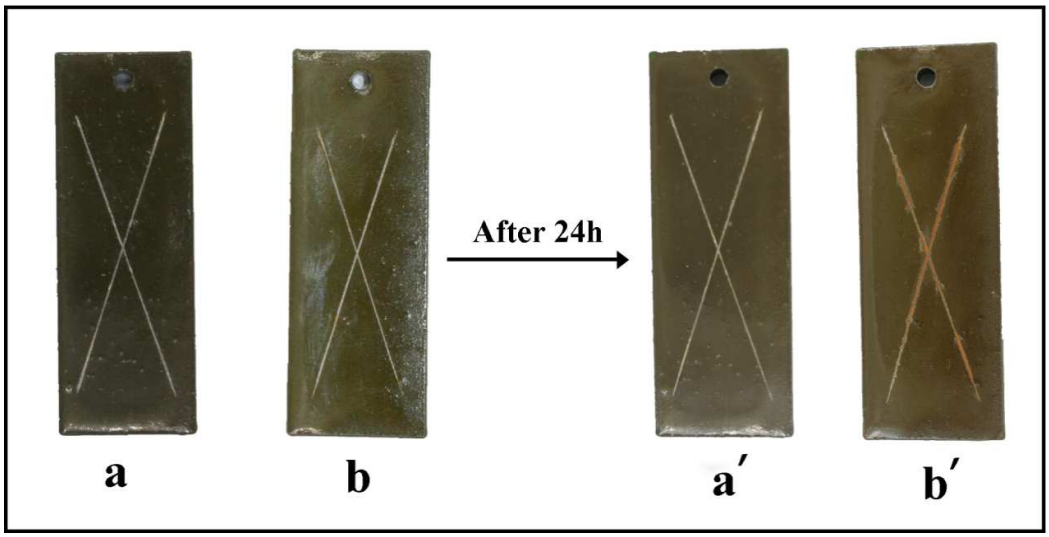

Figure 14

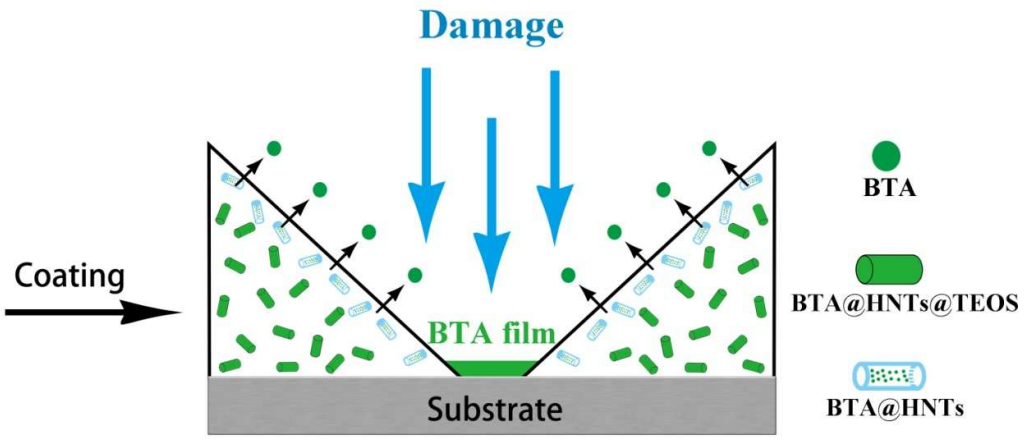
Damage
Coating
BTA film
Substrate
BTA
BTA@HNTs@TEOS
BTA@HNTs

Scheme 2

Table1. Changs in the chemical structure of the surface of nanotubes

		Al-O-H	Si-O-Si		$-NH_2$	$-NH_2/-NH-/NH_3^+$			
Sample	**O1s(at%)**	**531.7eV**	**532.6**	**N1s(at%)**	**399.4eV**	**401.5eV**	**Si(at%)**	**Al(at%)**	**C(at%)**
HNTs@TEOS	62.15	32.87	67.13	-	-	-	13.80	9.40	14.64
HNTs@TEOS-APTES	34.74	21.14	78.86	4.71	62.19	37.81	10.91	3.18	46.47

Table 2. The impedance parameters of coating after different periods of immersion

Immersion time(h)	R_{coat} (Ωcm^2)	Q_{coat}($\Omega^{-1}cm^{-2}s^n$)	n_{coat}	R_{film} (Ωcm^2)	C_{film}(Fcm^{-2})
12	11170	9.228×10^{-6}	0.7563	1431	4.242×10^{-4}
24	10320	9.991×10^{-6}	0.7762	1264	4.242×10^{-4}
48	8469	1.478×10^{-5}	0.8134	1400	4.164×10^{-4}
72	8314	1.890×10^{-5}	0.8255	1840	3.872×10^{-4}
102	7985	2.677×10^{-5}	0.8163	1893	5.594×10^{-4}
132	7889	2.956×10^{-5}	0.8191	1784	6.506×10^{-4}
162	6824	3.378×10^{-5}	0.8165	1354	8.136×10^{-4}
192	6132	4.484×10^{-5}	0.7878	841	1.551×10^{-3}